Lava lake sloshing modes during the 2018 Kīlauea Volcano eruption probe magma reservoir storativity

Chao Liang[a,*], Eric M. Dunham[a,b]

[a] *Department of Geophysics, Stanford University*
[b] *Institute for Computational and Mathematical Engineering, Stanford University*

Abstract

Semi-permanent lava lakes, like the one at the summit of Kīlauea Volcano, Hawai'i, provide valuable opportunities for studying basaltic volcanism. Seismic events recorded by the summit broadband seismometer network during the May 2018 eruption of Kīlauea feature multiple oscillatory modes in the very long period (VLP) band. The longest period mode (∼30-40 s, here termed the conduit-reservoir mode) persisted during drainage of the lava lake, indicating its primary association with the underlying conduit-reservoir system. Additional modes, with periods of 10-20 s, vanished during lake drainage and are attributed to lava lake sloshing. The surface displacements of the two longest period sloshing modes are explained as the superimposed response to a near-surface horizontal force along the axes of the crater (from the pressure imbalance during sloshing on the crater walls) and a volume change in a reservoir located at the conduit-reservoir mode source centroid. Both sloshing modes are in the "deep-water" surface gravity wave limit where disturbances are largest near the lake surface, though pressure changes on the top of the conduit at the lake bottom provide the observed excitation of the underlying conduit-reservoir system. Combining magma sloshing dynamics in the crater and a conduit-reservoir oscillation model, we bound the storativity of the reservoir (volume change per unit pressure change) to be greater than 0.4 m^3/Pa, probably indicating the presence of other shapes of magma bodies (than a spherical reservoir), such as sills or dikes, and/or significant finite source effect. Our work demonstrates the signature of lava lake sloshing modes in the seismic data and the potential of these modes in constraining the shallow magmatic system.

Keywords: Lava lake, magma sloshing, magma reservoir storativity, very long period (VLP), Kīlauea, 2018 May eruption

*Corresponding author
Email addresses: chaovite@gmail.com (Chao Liang), edunham@stanford.edu (Eric M. Dunham)

1. Introduction

Several open-vent volcanoes, such as Kīlauea Volcano, Hawai'i, and Mount Erebus, Antarctica, support semi-permanent lava lakes, providing valuable opportunities for studying basaltic volcanism (e.g. Aster et al., 2003; Patrick et al., 2011, 2018). As the uppermost part of the magmatic system, the lava lake, with directly observable outgassing and surface convection, offers insights into processes occurring in the deeper plumbing system (e.g. Chouet et al., 2010; Patrick et al., 2011, 2015; Anderson et al., 2015).

At the summit of Kīlauea Volcano, the Overlook crater was formed on the south wall of Halema'uma'u crater during an explosion in March 2008 (Wilson et al., 2008), as shown in Figure 1a, and subsequently expanded due to collapses of the crater wall (Patrick et al., 2018). The satellite image from Google Maps (image date: December 7, 2017) indicates a crater size of ∼270×190 m, as shown in Figure 1b. Sporadic bubble bursts and rockfalls on the lava lake excite oscillations in the very long period (VLP) band, 2-100 s, which have been attributed to various resonances in magma-filled cracks (e.g., Chouet, 1986; Ferrazzini and Aki, 1987), reservoirs (e.g., Shima, 1958), conduits (e.g., Garces, 2000; Karlstrom and Dunham, 2016), and coupled conduit-reservoir systems (e.g., Chouet and Dawson, 2013; Liang et al., 2019a). However, relatively less attention has been given to magma oscillations in the lava lake itself.

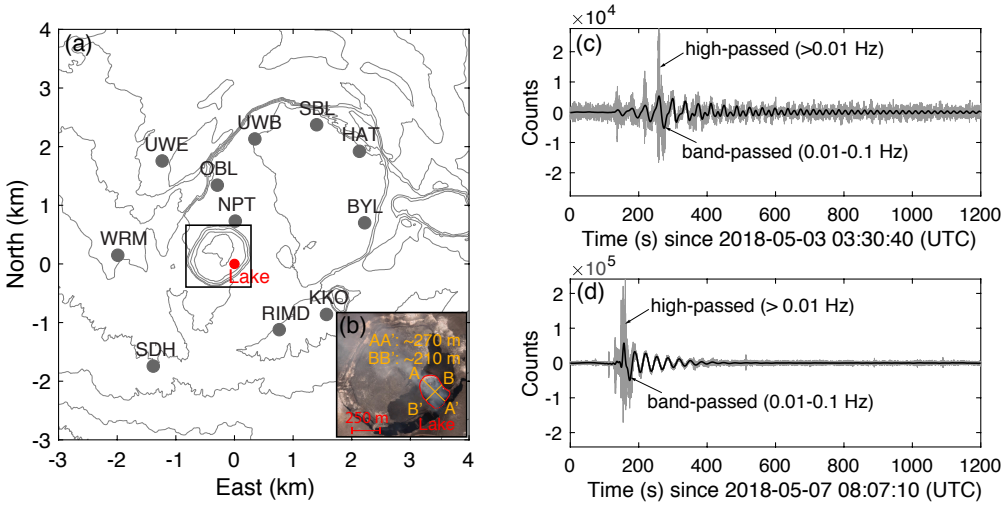

Figure 1: (a) Map of Kīlauea summit caldera showing broadband seismic stations and lava lake. (b) Zoomed-in view of the Halema'uma'u crater and the lava lake with semi-major and semi-minor axes marked as AA' (∼270 m) and BB' (∼190 m), obtained from Google Maps (image date: December 7, 2017). (c-d) NPT vertical velocities in raw counts for two events. The instrument response is nearly flat in the frequency band of interest.

Standing surface gravity waves in bounded ponds, channels, or locally isolated parts of basins give rise to fluid oscillations, commonly referred to as seiches

in the field of hydrodynamics (e.g., Wilson, 1972; Rabinovich, 2010). Seiches in water bodies can be driven by atmospheric pressure variations (Gomis et al., 1993), wind drag (Horn et al., 1986), seismic waves (McGarr, 1965), and landslides (Kulikov et al., 1996), for example. Water seiches have also been observed seismically (e.g., McNamara et al., 2011; Amundson et al., 2012) and by borehole strain meters (Luttrell et al., 2013). However, there have been relatively few reports of seiches, or sloshing (a synonymous term that we adopt in this study), in lava lakes. Notable exceptions are works by Richardson and Waite (2013) and Dawson and Chouet (2014). Richardson and Waite (2013) attribute the seismic source mechanism of a long period (LP) bubble burst event to the viscous drag of sloshing magma on the crater floor at Villarica Volcano. When characterizing VLP seismicity at Kīlauea Volcano during 2007-2013, Dawson and Chouet (2014) discovered two oscillation modes with periods of 10-20 s and hypothesized them to be lake sloshing modes along the two axes of the roughly elliptical-shaped crater. However, stronger evidence is required to rule out the possibility that these modes are due to other mechanisms such as crack wave resonance in shallow dikes or sills, or resonances in the conduit.

In this work, we present a comprehensive investigation of lava lake sloshing modes with periods of ∼10-20 s during the May 2018 eruption of Kīlauea Volcano. During the first ten days of May, the summit lava lake level dropped by more than 300 m (Neal et al., 2019). The evolution of seismic waveforms and spectra associated with the events as the lava lake drained from the crater provides strong evidence that the ∼10-20 s resonant modes are due to lake sloshing. We then show that the surface deformation of the two longest period sloshing modes are well explained by a combination of a near-surface horizontal force, resulting from the imbalance of pressure on the side walls of the crater as the lake lava sloshes, and a volume change of a shallow magma reservoir. The synchronization of these deformation sources requires hydraulic connection between the lake and reservoir, and motivates application of a coupled lake-conduit-reservoir model, an extension of the conduit-reservoir model introduced in Liang et al. (2019a), in interpreting the data. Using this model, we introduce a workflow to constrain the reservoir storativity (volume change per unit pressure change) from the inverted force and reservoir volume change. In this study, we adopt a 2D crater geometry when calculating the depth-dependent pressure distribution of the sloshing modes, but the approach should be extended to 3D when the crater geometry is publicly available.

2. Observation

The summit of Kīlauea Volcano is instrumented with a network of 11 broadband seismic stations (Figure 1a). We compile a dataset of 24 events (Liang and Dunham, 2019) by visually inspecting the raw waveforms at NPT station (see also Supplementary Material). These events are clearly visible in the seismograms, with high frequency peaks followed by VLP oscillations and positive up first motions, as exemplified by the two events shown in Figure 1c and 1d.

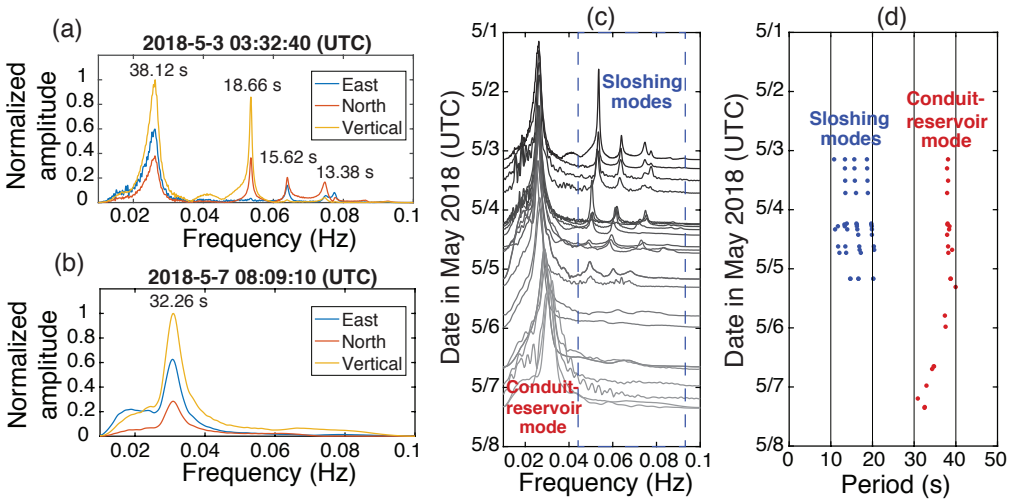

Figure 2: (a) NPT displacement spectra (normalized by the maximum spectral amplitude of the vertical component) of the event shown in Figure 1c. Note the distinct relative amplitudes of different components (East, North, and Vertical) for multiple resonant modes. (b) Same as (a) but for the event shown in Figure 1d. Note that this event only exhibits a single spectral peak around 32.26 s. (c) Total displacement spectra (Euclidean norm of the spectral amplitudes of three components) at NPT station between 3-8 May 2018. The gradual diminishing of modes in the 10-20 s band as the lava lake drained indicates their primary association with the lake. (d) Periods of identified spectral peaks.

The waveforms and spectral characteristics of these events change dramatically as the lava lake drained from the crater. When the lava lake level was high, multiple resonant modes were excited in the band of 10-100 s, as in the event on 3 May shown in Figures 1c and 2a. The longest oscillation period is ∼30-40 s, which matches the mode studied by Chouet et al. (2010), Dawson et al. (2010), and Chouet and Dawson (2013). As in Liang et al. (2019a), we refer to this mode as the conduit-reservoir mode. Higher modes in the 10-20 s band exhibit distinct relative amplitudes among the different components (East, North, and vertical) compared to the conduit-reservoir mode, as shown in Figure 2a. For example, the 18.66 s mode does not contain much East component while the 15.62 s mode lacks energy in the vertical component.

As shown in Figure 2c, the conduit-reservoir mode persists as the lake drains, indicating the mode's primary association with the underlying conduit-reservoir system. This observation is consistent with previous studies (Chouet and Dawson, 2013; Liang et al., 2019a), which explain this mode as oscillation of magma in a conduit beneath the lake with restoring force from buoyancy in the conduit and compressibility/storativity of a reservoir at the base of the conduit. Thus, the change of period of the conduit-reservoir mode from 38-40 s on 3 May to 30-32 s on 7 May (Figure 2d) indicates evolution of magma density and viscosity in the conduit-reservoir system, provided that the geometry is relatively fixed.

On the other hand, the higher modes in the 10-20 s band gradually diminish

as the lake level drops, indicating a primary association with the lava lake. By the end of 5 May, no observable spectral peaks are present in the 10-20 s band. For example, the 7 May event shown in Figure 1d and 2b exhibits only a single mode (the conduit-reservoir mode) with a period of ∼32 s. We can immediately rule out acoustic resonances within the lava lake as an explanation for the 10-20 s period modes as follows. Given the dimension of the lava lake (∼300 m), it would require a magma acoustic wave speed of ∼20 m/s to explain a ∼15 s oscillation, which is inconsistent with even order of magnitude constraints on density and compressibility of basaltic magma. As we will show later, these modes are instead well explained by lava lake sloshing, that is, the resonance of surface gravity waves on the lake surface. We therefore refer to the modes in the 10-20 s band as the "sloshing modes." Possible causes for the diminishing of sloshing modes as the lava lake drains will be presented following a more detailed explanation of the sloshing model.

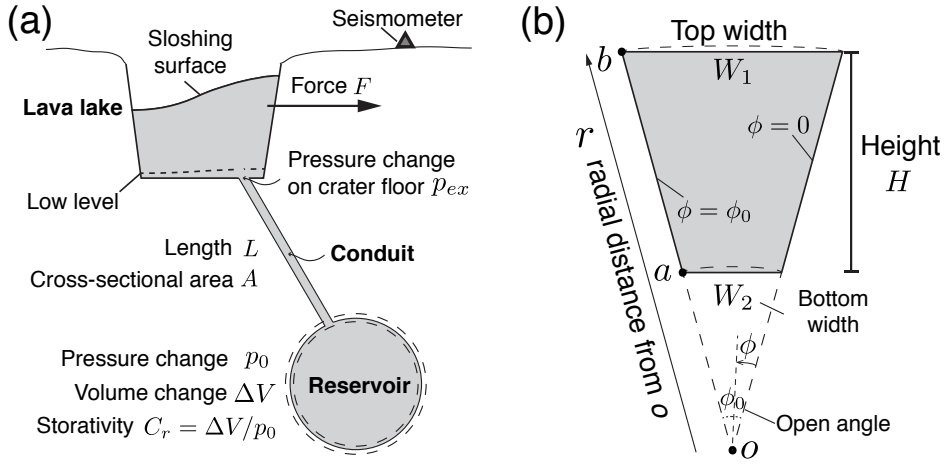

Figure 3: (a) Schematic of the magmatic system. Sloshing of the lava lake surface creates pressure perturbations in the lake, appearing as a horizontal force F exerted on the side walls of the crater and a pressure perturbation on the crater floor p_{ex} that drives oscillations of the underlying conduit-reservoir system and volume change ΔV in the reservoir. Both the horizontal force F and reservoir volume change ΔV contribute to the surface displacements. (b) Truncated wedge as an approximate 2D crater model, used in lake sloshing calculations.

3. Modeling surface deformation

In this section, we model the surface displacements of the conduit-reservoir mode and the two longest period sloshing modes (18.66 s and 15.68 s) for an event that occurred at 03:32:40 (UTC) on 3 May 2018, as shown in Figures 1c and 2a. This event occurred when the lava lake level was high with efficient coupling between the lava lake and the surrounding walls of the crater. Due to the very long period nature of these modes, we assume quasi-static solid

deformation. This assumption is valid when $\omega r/c \ll 1$, where ω is the angular frequency of oscillation, r is the source-receiver distance, and c is an elastic wave speed.

The reservoir location is well indicated by the deformation centroid of the conduit-reservoir mode, assuming negligible contributions to displacements from pressure changes within the narrow conduit following Liang et al. (2019b). For simplicity, we model the reservoir as a spherical magma reservoir, known as the Mogi source (Mogi, 1958). This assumption should not be interpreted as our preference for a spherical reservoir as opposed to other shapes such as cracks (sills or dikes). Instead, the Mogi source provides a minimal parameter model that permits quantitative estimation of the reservoir centroid location and volume change.

In the two longest period sloshing modes, the oscillating lava lake surface perturbs the pressure distribution inside the crater. The imbalance of pressure on the crater wall results in a net horizontal force, F (Figure 3a). The pressure change on the crater floor, p_{ex}, drives magma flow in/out of the reservoir through the conduit. Therefore, we model the surface displacements of the two sloshing modes as a combination of a horizontal force and a volume change in the reservoir. We use the Green's function for surface displacements due to a point force inside a uniform elastic half-space by Mindlin (1936). Antisymmetric pressure perturbations on the crater floor give rise to a vertical force couple, but this has negligible contribution to the surface displacement as compared to the horizontal force (see Supplementary Material) and is neglected. Likewise, the contributions to surface displacement from pressure changes on the walls of the conduit are negligible.

We also neglect topographic corrections to the Green's functions, though such corrections might be important to consider in future studies as pointed out by Johnson et al. (2019). The leading order topographic correction to the surface displacement is of order the surface slope times the surface displacement in an elastic half-space (McTigue and Segall, 1988; Segall, 2010). The surface slopes in the vicinity of the seismometers are generally 4% to 12%, suggesting an error of approximately 10%. This error is tolerable relative to other approximations we make such as our idealization of the crater shape and uncertainties in conduit location that are described in the next section.

We first invert the displacements of the conduit-reservoir mode of all events using a Mogi model to determine the location (East, North, and depth) of the magma reservoir. The deformation source centroid of the conduit-reservoir mode is remarkably stable over the entire lava lake drainage (Figure 4). Therefore, we fix the magma reservoir at the average conduit-reservoir mode source centroid and then invert the displacements of the two sloshing modes of the selected event for the amplitude $\hat{F}$, orientation θ (angle from North), and depth d of the horizontal point force, and the reservoir volume change $\Delta\hat{V}$. $\hat{F}(\omega)$ and $\Delta\hat{V}(\omega)$ are the spectral amplitudes of the time domain quantities $F(t)$ and $\Delta V(t)$. Note that the inversions are performed in the Fourier domain and only at frequencies of the resonant modes.

Following Maeda et al. (2011) and Chouet and Dawson (2013), we account

for the contribution of tilt to horizontal displacements, which can be substantial at very long periods. Because the surface displacement from a Mogi source is independent of the shear modulus G and the inverted $\hat{F}$ is proportional to G (Mindlin, 1936; Mogi, 1958), it is only possible to constrain $\hat{F}/G$. In this study, we assume $G = 10$ GPa and a Poisson ratio $\nu = 0.25$.

We apply the same processing technique introduced in Liang et al. (2019b) to the surface displacement data. To prepare the data for inversion, we extract, for each mode, the spectral values of displacements U_i, normalize by $e^{i\Phi_0}$, where Φ_0 is the phase of a reference channel (NPT vertical), and keep the real parts u_i. Note that i is the channel index. The fraction of the imaginary part I_i in the total amplitude a_i is an indication of deviation from the quasi-static assumption or noise. We compute the noise spectra n_i using a window of 500 s prior to the start time of the event and then obtain the signal-to-noise ratios $SNR_i = a_i/|n_i|$. For quality control, we discard the channels with $|I_i^2/a_i^2| > 0.1$ or $SNR_i < 5$.

The Markov Chain Monte Carlo (MCMC) method is used to estimate the posterior distributions of model parameters accounting for data uncertainty (e.g. Mosegaard and Tarantola, 1995). We assume flat priors with large bounds and a Gaussian likelihood function. Data uncertainty is estimated based on the SNR. Although SNR_i of most channels is above 10, we set the standard deviation of the displacement σ_u in each channel to be $\min(10, SNR_i) \times \max(a_i)$. This choice of standard deviation tends to overestimate the data uncertainty for channels with smaller amplitudes and is thus more robust with noisy data. In this study, we use an affine invariant ensemble MCMC sampler developed by Goodman and Weare (2010) to obtain one million samples with 50 random walkers. The software used, GWMCMC, is an open source repository on GitHub (Grinsted, 2014). Since we focus on modeling the deformation, the periods and decay rates are not used in the inversion.

3.1. Conduit-reservoir mode and reservoir location

The source centroid of the conduit-reservoir mode is well constrained as indicated by the 90% credible intervals in Figure 4. The general deformation pattern of the conduit-reservoir mode is vertical uplift/depression and horizontal expansion/contraction, consistent with a volumetric source (Mogi model in this study) as shown in Figure 4e. The displacement patterns of this mode are also highly consistent across different events, as shown in Figure 4d. As a result, the maximum likelihood estimate (MLE) of the source centroid is consistently located at ∼1 km depth, ∼660 m East, and ∼400 m North from the centroid of the vent during the entire lava lake drainage, as shown in Figures 4a, 4b, and 4c. This centroid location is at a similar depth with but ∼200 m east from the centroids previously inferred for events prior to 2013 (Chouet et al., 2010; Chouet and Dawson, 2013; Liang et al., 2019b) and is consistent with the centroid depth of the shallow magma reservoir participating in deflation-inflation (DI) events (Anderson et al., 2015).

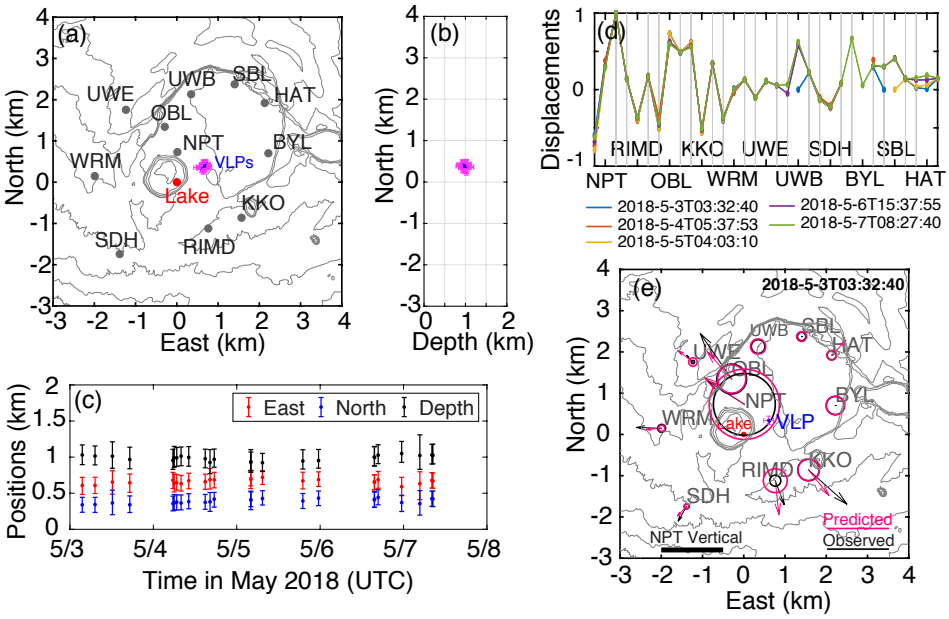

Figure 4: Inversion of the conduit-reservoir mode for event on 2018-5-3T03:32:40. (a) Horizontal and (b) North and depth positions of source centroids. The blue dots mark the maximum likelihood estimate (MLE) positions and the magenta error bars mark the 90% credible interval. (c) Centroid positions over time. Dots mark the MLEs and error bars mark the 90% credible interval. (d) Displacements u_i (after normalization by NPT vertical) for 5 events. The displacements are ordered by East, North and vertical from left to right for each station. Channels with I_i^2/a_i^2 >0.1 or SNR_i <5 are discarded. (e) Predicted (from the MLE model) and observed displacements. The diameters of circles indicate the vertical uplifts and arrows indicate horizontal displacements. The horizontal components of BLY, SBL, and UWB are discarded due to poor quality.

3.2. Lake sloshing modes

The results for inverting the two longest period lake sloshing modes of one event (start time 2018-5-3T03:32:40) are presented in Figure 5. For both sloshing modes, the angle θ, force amplitude $\hat{F}$, and reservoir volume change $\Delta\hat{V}$ are well constrained. In particular, the MLE of θ for two sloshing modes (18.66 s and 15.68 s) are 136.9° and 49.8° from the North, respectively, corresponding to directions along the major and minor axes of the Overlook crater, as shown in Figure 5a and c. The depth d of the horizontal force is not well constrained but the data seem to favor a shallower depth, which is likely related to the depth-dependence of pressure perturbations in the lake. Figure 5b and d show fits of the MLE models to observed displacements when fixing the reservoir location at the conduit-reservoir mode centroid for the two lake sloshing modes. Both the horizontal force and the reservoir volume change contribute to the surface deformation of the sloshing modes. As a horizontal point force is not effective at generating vertical displacements, the vertical displacements are largely con-

trolled by the reservoir volume change. Compared to the 18.66 s mode, the 15.68 s mode's displacements exhibit a higher contribution from the horizontal force than from the volumetric source. This is probably due to a larger contact area on the crater side walls perpendicular to the minor axis and smaller pressure perturbation at the crater floor due to smaller width-to-depth ratio to drive reservoir volume changes, as we demonstrate in the next section.

4. Inferring magma reservoir storativity

During lava lake sloshing, pressures within the lake are perturbed by the motion of the lake surface. This perturbation creates an imbalance of pressure on the crater walls that results in a net horizontal force along the crater axis pointing to the side with higher lake height. At the same time, the pressure perturbation on the crater floor drives magma into and out of the reservoir through the conduit, generating a volumetric component in the surface displacements. In this study, we propose a novel way to constrain the pressure-volume relation of the reservoir using the point force $\hat{F}$ and change in volume $\Delta\hat{V}$ obtained in the previous section.

Given a reservoir having pressure-dependent volume $V_r(p)$, we define the reservoir storativity C_r as

$$C_r \equiv dV_r/dp = \beta_r V_r = \Delta V/p_0, \tag{1}$$

where β_r is reservoir compressibility, ΔV is the change in reservoir volume, and p_0 is the perturbation of reservoir pressure. Equation (1) holds for both the time and frequency domain. Note that C_r solely accounts for the compressibility of the reservoir itself, β_r, but not magma compressibility $\beta_m = \rho_m^{-1} d\rho_m/dp$, where $\rho_m(p)$ is pressure-dependent magma density. The total storativity that accounts for both β_r and β_m is defined as (e.g. Anderson et al., 2015; Rivalta and Segall, 2008)

$$C_t = \Delta V_{in}/p_0 = (\beta_r + \beta_m)V_r, \tag{2}$$

where ΔV_{in} is the magma volume injected into the reservoir. Due to finite magma compressibility, $\Delta V_{in} \geq \Delta V$, such that $C_r \leq C_t$. For the ease of later discussion, we denote $\hat{p}_0(\omega)$ as the Fourier transform of $p_0(t)$. The pressure perturbation at the floor of the crater (or the top of the conduit) is defined as $p_{ex}(t)$ with Fourier transform $\hat{p}_{ex}(\omega)$.

Conventional geodetic inversions using volumetric sources only constrain the reservoir volume change and alternative observations are necessary to obtain the reservoir pressure change (e.g. Anderson et al., 2015). In this study, we demonstrate how the obtained $\hat{F}$ puts constraints on $\hat{p}_0$, which then constrains C_r given the estimate of $\Delta\hat{V}$. We break this task into two steps. The first step is to convert $\hat{F}$ to the pressure perturbation at the floor of the crater $\hat{p}_{ex}$, which involves modeling the sloshing dynamics in the lava lake. The second step relates $\hat{p}_{ex}$ to $\hat{p}_0$ using an oscillation model for the conduit-reservoir system.

4.1. Lava lake sloshing dynamics

To relate the inverted horizontal force $\hat{F}$ and convert it to the pressure change on the lake bottom (crater floor) $\hat{p}_{ex}$ that forces the underlying conduit-reservoir system, we must understand the spatial distribution of pressure perturbation within the crater during lava lake sloshing. In the current study, we model the crater as a 2D truncated wedge as shown in Figure 3b. The wedged face is defined by the region with $a \leq r \leq b$ and $0 \leq \phi \leq \phi_0$, where r is radial distance from the apex and ϕ is the angle counterclockwise from the right crater wall. The two subvertical walls are defined as $\phi = 0$ and $\phi = \phi_0$. $r = a$ and $r = b$ indicate the crater floor and free surface, respectively. The two sloshing modes are assumed to be independent and modeled with different truncated wedge geometries.

We use the surface gravity wave solutions by Bauer (1981) for a 3D wedged tank with finite thickness filled with inviscid, incompressible fluid. The two longest period modes, which are the ones relevant to our application, have eigenfunctions that are independent of the thickness. The formulas for sloshing frequencies and pressure perturbations for the 3D truncated wedge (Bauer, 1981) and a 2D rectangular tank (e.g. Ibrahim, 2005) are given in the Supplementary Material. The method presented here can be straightforwardly extended to 3D by replacing the 2D eigenmode analysis with a 3D model.

The inviscid assumption in calculating resonant frequencies and pressure distribution is justified by realizing the sloshing modes are in the boundary layer limit. The thickness δ of viscous boundary layers along the crater walls scales as $\sqrt{\mu_m/(\rho_m\omega)}$, where μ_m is magma dynamic viscosity and ω is the angular frequency of oscillation. Given the sloshing mode period ≈20 s, basaltic magma density ≈1000 kg/m^3, and basaltic magma dynamic viscosity 1-1000 Pa s, we obtain δ ≈0.05-2 m, which is much smaller than the depth of the lava lake. Therefore, the boundary layer limit is justified and viscosity is neglected in calculating the period and pressure distribution of the sloshing modes.

The Overlook crater is $\sim 270 \times 190$ m at the top (Figure 1b) and ∼300 m deep as revealed by the 2018 May eruption (Neal et al., 2019). According to Neal et al. (2019), the average rate of lava lake drop was ∼30 m/day between 1-10 May. However, the withdrawal only accelerated after the M_w 6.9 earthquake on 4 May. Assuming the lava lake level dropped ∼30 m during the first two days of May, we estimate a lake depth of ∼270 m for the studied event on 3 May. The bottom part of the crater is approximately elliptical with dimension of $\sim 160 \times 140$ m as revealed by the lava lake withdrawal in March 2011 (Carbone et al., 2013). Therefore, we use $W_1 = 270$ m, $W_2 = 160$ m, and $H = 270$ m for the 18.68 s mode, and $W_1 = 190$ m, $W_2 = 140$ m, and $H = 270$ m for the 15.62 s mode.

The predicted periods for the two sloshing modes using the truncated wedge model are 18.61 s and 15.61 s, matching the observed periods 18.66 s and 15.62 s remarkably well. In fact, the predicted periods from rectangular tanks with shapes $W_1 = W_2 = 270$ m, $H = 270$ m and $W_1 = W_2 = 190$ m, $H = 270$ m are 18.64 s and 15.61 s, which are very close to predictions from the truncated

wedge model. This observation indicates that both sloshing modes are in the short wavelength or "deep-water" limit where the resonant periods are only sensitive to the crater dimension at the top and relatively insensitive to the depth (e.g. Ibrahim, 2005).

The pressure perturbations, as shown in Figure 6a and b, are depth-dependent and concentrated near the free surface, reaffirming that both sloshing modes are in the short wavelength limit. For both sloshing modes, the pressure perturbations on the crater floor are substantially less than (<5% of) those at the top and can vary significantly depending on the horizontal position (highest near the wall and zero at the nodal point). In addition, the bottom geometry of the crater has substantial impact on the pressure distribution near the crater floor (see Supplementary Material).

From the spatial distribution of pressure perturbation, we compute the horizontal force $\hat{F}$ and the pressure perturbation $\hat{p}_{ex}$ at a given position on the crater floor. To calculate $\hat{F}$ due to sloshing along one crater axis, we resolve the depth-dependent pressure profile into tractions on the crater wall ($\phi = 0$), the wedged cross-section perpendicular to this axis. The azimuthal dependence of pressure perturbation would have to be taken into account if a 3D crater geometry were used. $\hat{p}_{ex}$ is directly evaluated given the position of the conduit on the crater floor. We now compute the ratio $\hat{F}/\hat{p}_{ex}$, in which undetermined constants drop out. Since $\hat{p}_{ex}$ depends on the position of the conduit on the crater floor, which is poorly known, we evaluate $\hat{p}_{ex}$ at $\phi = 0$, giving an upper bound estimate of $\hat{p}_{ex}$. The computed $\hat{p}_{ex}/\hat{F}$ of the two sloshing modes (18.66 s and 15.62 s) are 1.3×10^{-6} m^{-2} and 2.4×10^{-6} m^{-2}, respectively.

Now that we have introduced the sloshing model, we offer possible explanations for the diminishing seismic expression of the sloshing modes as the lake level drops, as seen in Figure 2c. One possibly important factor is the reduction of contact area between the magma and the crater walls as the lake drains and the crater narrows with depth. The reduction of contact area directly reduces the horizontal force on the crater wall even when the lava lake surface is perturbed by the same amount. Another possibly important factor could be viscosity, which bounds the amplitude of the lake sloshing response to external forcing around the resonant frequencies (e.g. Ibrahim, 2005). As the lava lake gets shallower, cooler and thus more viscous magma is in contact with the crater walls and floor. Additionally, the ratio of viscous boundary layer thickness to lake depth increases, which increases damping. Together, all of these effects will contribute to weaker seismic expression as the lake drains, which is confirmed by the increase of spectral widths in Figure 2c and slight increase of periods in Figure 2d. Extension of our lake model to a viscous fluid is required to quantify these effects and demonstrate consistency with the observations.

4.2. Oscillation of the conduit-reservoir system

We use the conduit-reservoir oscillation model developed in Liang et al. (2019a), to relate $\hat{p}_{ex}$ to $\hat{p}_0$. This model accounts for two restoring forces: buoyancy in the conduit and reservoir pressure changes from compressibility of the reservoir and magma within it. We introduce the governing equation of the

oscillator for inviscid magma here, for simplicity, and leave the treatment of viscosity in the Supplementary Material. The viscous magma model is used in actual calculations because the viscous boundary layer thickness can be comparable to the conduit radius, which is on the order of a few meters (Fee et al., 2010).

Consider oscillation of incompressible, inviscid magma in a vertical cylindrical conduit of length L and cross-sectional area A, as shown in Figure 3a. The governing equation for the vertical displacement of the magma column, h, is

$$\frac{d^2h}{dt^2} + \frac{A}{\rho_m L C_t} h + \frac{\Delta\rho g}{\rho_m L} h = -\frac{p_{ex}}{\rho_m L}, \tag{3}$$

where ρ_m is magma density, $\Delta\rho$ is the magma density contrast between the bottom and the top of the conduit, C_t is the total storativity defined in (2), and p_{ex} is the external pressure perturbation at the top of the conduit. The second and third terms on the left-hand side of (3) represent the restoring force from reservoir pressure perturbation $p_0 = -Ah/C_t$ and buoyancy. This is essentially a spring-mass system driven by external forcing from p_{ex}, with the spring being the restoring force from the reservoir and buoyancy and the mass being the total magma mass in the conduit. The relative significance between the two restoring forces is quantified by the stiffness ratio

$$\gamma = \frac{AC_t^{-1}}{\Delta\rho g}. \tag{4}$$

When $\gamma \gg 1$, reservoir stiffness dominates the restoring force over buoyancy, and vice versa. The inviscid free oscillation angular frequency is

$$\omega_0 = \sqrt{A(1 + 1/\gamma)/\rho_m L C_t} \tag{5}$$

and the natural period is $T_0 = 2\pi/\omega_0$. We can rewrite (3) in terms of p_0 as

$$\omega_0^{-2} d^2p_0/dt^2 + p_0 = \frac{\gamma}{1+\gamma} p_{ex}. \tag{6}$$

Equation (6) can be solved in the frequency domain, giving

$$\frac{\hat{p}_0}{\hat{p}_{ex}} = \frac{\gamma}{1+\gamma} \frac{1}{1 - (\omega/\omega_0)^2}, \tag{7}$$

where ω is angular frequency. As buoyancy becomes increasingly important relative to reservoir stiffness, the reservoir pressure change per unit external pressure change at the top of the conduit decreases, as indicated by this ratio $\gamma/(1+\gamma)$. Thus, neglecting buoyancy ($\gamma^{-1} = 0$) results in an upper bound estimate of $\hat{p}_0$. We note that this upper bound could be an dramatic overestimation if buoyancy dominates the restoring force; analysis of the conduit-reservoir mode by Liang et al. (2019b), suggests $\gamma \sim 0.1$. Nonetheless, in this study we proceed by neglecting buoyancy (that is, setting $\gamma^{-1} = 0$) to obtain a lower bound estimate of reservoir storativity and then later discuss how results and conclusions might

change if the system is in the buoyancy-dominated limit. $\hat{p}_0/\hat{p}_{ex}$ is amplified when $\omega \approx \omega_0$, converges to 1 as $\omega/\omega_0 \to 0$, and decays to -0 as $\omega/\omega_0 \to \infty$. The sign of $\hat{p}_0/\hat{p}_{ex}$ changes from positive to negative as ω exceeds ω_0. When the system is driven with $\omega > \omega_0$, $p_0(t)$ and $p_{ex}(t)$ are out of phase, such that when the top of the conduit is experiencing a positive pressure perturbation, the reservoir is deflating.

When viscosity μ_m is added, the free oscillation is damped, exhibiting a finite quality factor Q and a longer period T than T_0. Q is defined as the number of oscillations required for a free oscillation's energy to fall off to $e^{-2\pi}$ or $\sim$0.2% of its original energy (e.g. Green, 1955). Given T and Q, ω_0 (or T_0) can be obtained and $\hat{p}_0/\hat{p}_{ex}$ can be solved as a function of ω/ω_0 (see Supplementary Material).

As shown in Figure 7, $\hat{p}_0/\hat{p}_{ex}$ with viscosity has a finite amplitude and non-real component near ω_0 but otherwise very similar characteristics with the inviscid limit away from ω_0. The event with start time 2018-5-3T03:32:40 has a conduit-reservoir mode with $T = 38.12$ s and $Q = 11$, which we interpret as the free oscillation of the conduit-reservoir system. The obtained T_0 is 36.53 s, slightly smaller than T. Pressure perturbations $\hat{p}_{ex}$ from the two sloshing modes (18.66 s and 15.62 s) thus drive the underlying conduit-reservoir system into forced oscillations with frequencies higher than the natural frequency of the system. At the two sloshing mode periods (18.66 s and 15.62 s), $|\hat{p}_0/\hat{p}_{ex}|$ is 0.32 and 0.21, respectively, with opposite signs for the real parts of $\hat{p}_0$ and $\hat{p}_{ex}$. The reservoir storativity C_r is then obtained by equation (1) as

$$C_r = \frac{\Delta\hat{V}}{\hat{p}_0} = \left|\frac{\hat{p}_{ex}}{\hat{p}_0}\right| \times \left|\frac{\hat{F}}{\hat{p}_{ex}}\right| \times \frac{\Delta\hat{V}}{\hat{F}}. \tag{8}$$

The opposite signs of $\hat{p}_0$ and $\hat{p}_{ex}$ together with the displacement patterns help constrain the location of the conduit on the crater floor, as shown in Figure 8. For example, in the 15.62 s sloshing mode, when the horizontal force is pointing in the OB direction, the reservoir undergoes inflation with vertical surface uplift, as shown in Figures 5d and 8a. Inflation in the reservoir indicates a positive $\hat{p}_0$ and therefore a negative $\hat{p}_{ex}$ due to the phase lag. A horizontal force pointing in the OB direction indicates an increase of pressure in the ABA' half of the crater and a decrease of pressure in the $AA'B'$ half of the crater. Therefore, the 15.62 s sloshing mode constrains the conduit to the $AA'B'$ half of the crater. Similarly, the 18.66 s sloshing mode constrains the conduit to the ABB' half of the crater. Therefore, the conduit location is constrained in the AOB' quadrant of the crater, the green region in Figure 8a. This prediction is consistent with the vigorously convecting region in an image of the lava lake captured on 7 May 2019 when the lava lake level was near the bottom, as shown in Figure 8b, and also with the observed convective patterns on the lava lake surface in previous years (e.g., Patrick et al., 2018).

Although we have no direct constraints on the reservoir shape, we can estimate the reservoir dimensions for some end-member cases. For a spherical

reservoir, the diameter can be expressed as (e.g. Segall, 2010)

$$D = \left(\frac{8GC_r}{\pi}\right)^{1/3} = \left(\frac{8}{\pi}\left|\frac{\hat{p}_{ex}}{\hat{p}_0}\right| \times \left|\frac{\hat{F}}{\hat{p}_{ex}}\right| \times \frac{\Delta\hat{V}}{\hat{F}/G}\right)^{1/3}. \quad (9)$$

For a penny-shaped crack reservoir, the diameter can be expressed as (Sneddon, 1946)

$$D_c = \left(\frac{3GC_r}{1-\nu}\right)^{1/3} \approx 1.16D, \quad (10)$$

assuming $\nu = 0.25$. Note that C_r puts no constraints on the crack width. The diameter of a penny-shaped crack estimated from C_r is very similar to that of a spherical reservoir. Therefore, we only report the distribution of the diameter of a spherical reservoir.

Using the posterior samples of $\hat{F}$ and $\Delta\hat{V}$ obtained from the MCMC inversion, we construct the distribution of C_r and D. Since $\hat{F}/G$ is well constrained by displacements from the horizontal force, our estimate of D is robust with respect to shear modulus G. Since both $|\hat{p}_0/\hat{p}_{ex}|$ and $\left|\hat{p}_{ex}/\hat{F}\right|$ are upper bound estimates, the current method puts a lower bound on C_r and D.

4.3. Results

In Figure 9, we report reservoir storativity C_r and diameter D constrained by independent analysis of the two sloshing modes. The 18.66 s mode gives a C_r of about 0.46 m^3/Pa (MLE) with 90% credible interval of 0.39-0.59 m^3/Pa. The 15.62 s mode gives a C_r of about 0.09 m^3/Pa (MLE) with 90% credible interval of 0.04-0.10 m^3/Pa. As a result, the 18.66 s mode gives $D \approx 2.27$ km (MLE) with a 90% credible interval of 2.16-2.47 km. The 15.62 s mode gives $D \approx 1.31$ km (MLE) with a 90% credible interval of 1.03-1.39 km.

The apparent discrepancy of storativity and diameter of the same reservoir constrained by independent analyses of the two sloshing modes should not be viewed as a sign of contradiction. This is because we evaluate $\hat{p}_{ex}$ near the wall for both modes because of uncertainty in the exact conduit location, which results in a upper bound estimate for $\hat{p}_{ex}$ and lower bound estimates for C_r and D. If we shift the conduit location along the minor axis from the wall to 7 m from the center and keep the conduit near the wall along the major axis, we can get the MLEs of C_r and D from both sloshing modes to match, as shown in Figure 9 (the yellow and blue lines). Potentially, we could adjust the position of the conduit along both crater axes and obtain a set of positions where C_r from both sloshing modes match. In reality, however, the 3D crater geometry would have a significant impact on the pressure distribution on the crater floor. In this study, we thus focus on obtaining bounds for C_r using a 2D crater model rather than tuning the conduit location to obtain the exact C_r that is consistent for both sloshing modes. We recommend revisiting this analysis when the 3D crater geometry is publicly available.

Among the two lower bounds of C_r constrained by the two sloshing modes, we take the higher lower bound as the overall lower bound and hence constrain

C_r to be larger than $\sim$0.4 m^3/Pa. This bound is consistent with the estimates by Anderson et al. (2015) of 0.21-0.46 m^3/Pa with 95% confidence. The diameter D is thus constrained to be larger than $\sim$2.16 km for a spherical reservoir. If the reservoir is a penny-shaped crack, then its diameter $D_c \approx 1.16D$ and is longer than $\sim$2.5 km. However, if the restoring force for the conduit-reservoir oscillation is dominated by the buoyancy ($\gamma \ll 1$) as suggested by Liang et al. (2019b), then the actual C_r would need to much larger. For instance, a $\gamma \sim 0.1$ results in a ten-fold increase in C_r (to $\sim$4 m^3/Pa) and a 2.1 fold increase in D (to $\sim$ 4.6km).

Such large reservoir storativity places a significant constraint on the structure of the shallow magmatic system. A single sphere with diameter larger than 2.16 km (or even larger seems incompatible with the reservoir centroid depth $\sim$1 km. Several mechanisms neglected in this study may help to reconcile this geometric incompatibility. For a large and shallow reservoir, a Mogi model can significantly underestimate surface displacements (e.g., Segall, 2010). As a consequence, the reservoir size D (and its storativity) are overestimated. However, quantifying the finite source effect requires numerical calculations that are beyond the scope of the present study. On the other hand, a sub-horizontal sill could satisfy the geometric constraint, but is challenging to connect with the lava lake in a manner that is consistent with conduit-reservoir mode properties (Liang et al., 2019b). Alternatively, the observed storativity may be explained by a reasonably small spherical or ellipsoidal reservoir connected to sills or dikes that increase its storativity. Our estimate may also have been limited by the 2D crater geometry and revisiting these calculations with a 3D model is recommended.

5. Conclusion

Multiple oscillation modes in the VLP band are visible in seismic events during the May 2018 Kīlauea eruption. The mode with the longest period ($\sim$30-40 s) persists during the lava lake drainage, indicating its primary association with the underlying conduit-reservoir system. Modes with periods of 10-20 s are due to lava lake sloshing and disappear as the magma is drained from the crater. The surface displacements of two longest period sloshing modes are well explained by a horizontal force along the axes of the crater, arising from the imbalance of pressure perturbation on the crater walls, and a volume change at a magma reservoir. The periods of the two longest period sloshing modes are in excellent agreement with the predictions from surface gravity waves in the deep water limit given the crater dimension near the top ($\sim 270 \times 190$ m). In this limit, pressure perturbations are primarily confined near the free surface and crater shape has a significant control on the pressure perturbation on the crater floor.

We also introduced a method to constrain the magma reservoir storativity from observed seismic displacements of the two longest period sloshing modes. This involves converting the horizontal force into the change in reservoir pressure and volume using magma sloshing dynamics and a conduit-reservoir oscillation

model. The data constrain the storativity C_r of the summit magma reservoir at $\sim$1 km depth to be larger than $\sim$0.4 m^3/Pa, consistent with previous estimates in the literature. This lower bound on C_r is obtained due to two approximations: neglecting buoyancy in the conduit and evaluating $\hat{p}_{ex}$ near the crater wall. However, a purely spherical reservoir model seems problematic in reconciling the observed storativity and reservoir centroid depth, possibly indicating the presence of other magma bodies, such as sills and dikes connected to the magma reservoir.

The sloshing modes, with frequencies twice higher than the natural frequency of the conduit-reservoir system, drive the underlying conduit-reservoir system into forced oscillation. Due to the phase lag between the external forcing and response of damped harmonic oscillators at high frequencies, the pressure perturbation in the reservoir $\hat{p}_0$ is of opposite sign to the pressure perturbation at the crater floor $\hat{p}_{ex}$. A positive pressure change on the crater floor corresponds to deflation in the reservoir during these sloshing modes. This observation, together with surface displacement patterns, constrains the location of the conduit to the northwest to west quadrant of the crater, consistent with convective patterns on the lava lake surface.

Future studies could utilize the change of periods and decay rates of the sloshing modes to constrain the evolution of magma density and viscosity. This requires a rigorous treatment of viscosity during magma sloshing. More accurate 3D crater geometry and conduit location would also help to put tighter constraints on the storativity of the shallow magma reservoir at the summit of Kīlauea Volcano. Combination of different finite source models need to be tested to better interpret the obtained reservoir storativity. In addition, the sloshing lava lake surface may produce observable infrasonic signals, which could provide additional constraints on the lava lake sloshing dynamics.

References

Amundson, J.M., Clinton, J.F., Fahnestock, M., Truffer, M., Lüthi, M.P., Motyka, R.J., 2012. Observing calving-generated ocean waves with coastal broadband seismometers, Jakobshavn Isbræ, Greenland. Annals of Glaciology 53, 79–84. URL: https://doi.org/10.3189/2012/AoG60A200, doi:10.3189/2012/AoG60A200.

Anderson, K.R., Poland, M.P., Johnson, J.H., Miklius, A., 2015. Episodic Deflation-Inflation Events at Kīlauea Volcano and Implications for the Shallow Magma System. American Geophysical Union (AGU). chapter 11. pp. 229–250. URL: https://agupubs.onlinelibrary.wiley.com/doi/abs/10.1002/9781118872079.ch11, doi:10.1002/9781118872079.ch11.

Aster, R., Mah, S., Kyle, P., McIntosh, W., Dunbar, N., Johnson, J., Ruiz, M., McNamara, S., 2003. Very long period oscillations of Mount Erebus Volcano. Journal of Geophysical Research: Solid Earth 108. URL: https://agupubs.onlinelibrary.wiley.com/doi/abs/10.1029/2002JB002101, doi:10.1029/2002JB002101.

Bauer, H.F., 1981. Liquid oscillations with a free surface in wedge-shaped tanks. Acta Mechanica 38, 31–54.

Carbone, D., Poland, M.P., Patrick, M.R., Orr, T.R., 2013. Continuous gravity measurements reveal a low-density lava lake at Kīlauea volcano, Hawai'i. Earth and planetary science letters 376, 178–185. URL: https://doi.org/10.1016/j.epsl.2013.06.024, doi:10.1016/j.epsl.2013.06.024.

Chouet, B., 1986. Dynamics of a fluid-driven crack in three dimensions by the finite difference method. Journal of Geophysical Research: Solid Earth 91, 13967–13992. URL: https://doi.org/10.1029/JB091iB14p13967, doi:10.1029/JB091iB14p13967.

Chouet, B., Dawson, P., 2013. Very long period conduit oscillations induced by rockfalls at Kilauea Volcano, Hawaii. Journal of Geophysical Research: Solid Earth 118, 5352–5371. URL: https://agupubs.onlinelibrary.wiley.com/doi/abs/10.1002/jgrb.50376, doi:10.1002/jgrb.50376.

Chouet, B.A., Dawson, P.B., James, M.R., Lane, S.J., 2010. Seismic source mechanism of degassing bursts at Kilauea Volcano, Hawaii: Results from waveform inversion in the 10-50 s band. Journal of Geophysical Research: Solid Earth 115. URL: https://agupubs.onlinelibrary.wiley.com/doi/abs/10.1029/2009JB006661, doi:10.1029/2009JB006661.

Dawson, P., Chouet, B., 2014. Characterization of very-long-period seismicity accompanying summit activity at Kilauea Volcano, Hawai'i: 2007-2013. Journal of Volcanology and Geothermal Research 278-279, 59 – 85. URL: http://www.sciencedirect.com/science/article/pii/S0377027314001206, doi:https://doi.org/10.1016/j.jvolgeores.2014.04.010.

Dawson, P.B., Benítez, M.C., Chouet, B.A., Wilson, D., Okubo, P.G., 2010. Monitoring very-long-period seismicity at Kilauea Volcano, Hawaii. Geophysical Research Letters 37. URL: https://agupubs.onlinelibrary.wiley.com/doi/abs/10.1029/2010GL044418, doi:10.1029/2010GL044418.

Fee, D., Garcés, M., Patrick, M., Chouet, B., Dawson, P., Swanson, D., 2010. Infrasonic harmonic tremor and degassing bursts from Halema'uma'u Crater, Kilauea Volcano, Hawai'i. Journal of Geophysical Research: Solid Earth 115. URL: https://doi.org/10.1029/2010JB007642, doi:10.1029/2010JB007642.

Ferrazzini, V., Aki, K., 1987. Slow waves trapped in a fluid-filled infinite crack: Implication for volcanic tremor. Journal of Geophysical Research: Solid Earth 92, 9215–9223. URL: https://doi.org/10.1029/JB092iB09p09215, doi:10.1029/JB092iB09p09215.

Garces, M., 2000. Theory of acoustic propagation in a multi-phase stratified liquid flowing within an elastic-walled conduit of varying cross-sectional area.

Journal of volcanology and geothermal research 101, 1–17. URL: https://doi.org/10.1016/S0377-0273(00)00155-4, doi:10.1016/S0377-0273(00)00155-4.

Gomis, D., Monserrat, S., Tintoré, J., 1993. Pressure-forced seiches of large amplitude in inlets of the Balearic Islands. Journal of Geophysical Research: Oceans 98, 14437–14445. URL: https://doi.org/10.1029/93JC00623, doi:10.1029/93JC00623.

Goodman, J., Weare, J., 2010. Ensemble samplers with affine invariance. Communications in applied mathematics and computational science 5, 65–80. URL: https://doi.org/10.2140/camcos.2010.5.65, doi:10.2140/camcos.2010.5.65.

Green, E.I., 1955. The story of Q. American Scientist 43, 584–594.

Grinsted, A., 2014. GWMCMC: an implementation of the Goodman & Weare MCMC sampler for matlab. https://github.com/grinsted/gwmcmc.

Horn, W., Mortimer, C.H., Schwab, D.J., 1986. Wind-induced internal seiches in Lake Zurich observed and modeled 1. Limnology and Oceanography 31, 1232–1254. URL: https://doi.org/10.4319/lo.1986.31.6.1232, doi:10.4319/lo.1986.31.6.1232.

HVO, 2018. Halema‘uma‘u lava lake level continues to drop. https://volcanoes.usgs.gov/vsc/movies/movie_173941/multimediaFile-1973.mp4. Accessed: 2019-05-30.

Ibrahim, R.A., 2005. Liquid sloshing dynamics: theory and applications. Cambridge University Press.

Johnson, J.H., Poland, M.P., Anderson, K.R., Biggs, J., 2019. A cautionary tale of topography and tilt from Kīlauea caldera. Geophysical Research Letters 46, 4221–4229. URL: https://doi.org/10.1029/2018GL081757, doi:10.1029/2018GL081757.

Karlstrom, L., Dunham, E.M., 2016. Excitation and resonance of acoustic-gravity waves in a column of stratified, bubbly magma. Journal of Fluid Mechanics 797, 431–470. URL: https://doi.org/10.1017/jfm.2016.257, doi:10.1017/jfm.2016.257.

Kulikov, E.A., Rabinovich, A.B., Thomson, R.E., Bornhold, B.D., 1996. The landslide tsunami of November 3, 1994, Skagway harbor, Alaska. Journal of Geophysical Research: Oceans 101, 6609–6615. URL: https://doi.org/10.1029/95JC03562, doi:10.1029/95JC03562.

Liang, C., Karlstrom, L., Dunham, E.M., 2019a. Magma oscillations in a conduit-reservoir system, applications to very long period (VLP) seismicity at basaltic volcanoes–Part I: Theory. Journal of Geophysical Research: Solid Earth doi:10.1029/2019JB017437. in press.

Liang, C., Crozier, J., Karlstrom, L., Dunham, E.M., 2019b. Magma oscillations in a conduit-reservoir system, applications to very long period (VLP) seismicity at basaltic volcanoes–Part II: Data inversion and interpretation at kilauea volcano. Journal of Geophysical Research: Solid Earth doi:10.1029/2019JB017456. in press.

[dataset]Liang, C., Dunham, E., 2019. Dataset for lava lake sloshing modes during the 2018 Kilauea Volcano eruption. Zenode, v1.0, URL: https://doi.org/10.5281/zenodo.3525088, doi:10.5281/zenodo.3525088.

Luttrell, K., Mencin, D., Francis, O., Hurwitz, S., 2013. Constraints on the upper crustal magma reservoir beneath Yellowstone Caldera inferred from lake-seiche induced strain observations. Geophysical Research Letters 40, 501–506. URL: https://doi.org/10.1002/grl.50155, doi:10.1002/grl.50155.

Maeda, Y., Takeo, M., Ohminato, T., 2011. A waveform inversion including tilt: method and simple tests. Geophysical Journal International 184, 907–918. URL: https://doi.org/10.1111/j.1365-246X.2010.04892.x, doi:10.1111/j.1365-246X.2010.04892.x.

McGarr, A., 1965. Excitation of seiches in channels by seismic waves. Journal of Geophysical Research 70, 847–854. URL: https://doi.org/10.1029/JZ070i004p00847, doi:10.1029/JZ070i004p00847.

McNamara, D., Ringler, A., Hutt, C., Gee, L., 2011. Seismically observed seiching in the Panama Canal. Journal of Geophysical Research: Solid Earth 116. URL: https://doi.org/10.1029/2010JB007930, doi:10.1029/2010JB007930.

McTigue, D., Segall, P., 1988. Displacements and tilts from dip-slip faults and magma chambers beneath irregular surface topography. Geophysical Research Letters 15, 601–604. URL: https://doi.org/10.1029/GL015i006p00601, doi:10.1029/GL015i006p00601.

Mindlin, R.D., 1936. Force at a point in the interior of a semi-infinite solid. Physics 7, 195–202. URL: https://doi.org/10.1063/1.1745385, doi:10.1063/1.1745385.

Mogi, K., 1958. Relations between the eruptions of various volcanoes and the deformations of the ground surfaces around them. Bull. Earthquake Res Inst. Univ. Tokyo 36, 99–134. URL: https://ci.nii.ac.jp/naid/10017329458/en/.

Mosegaard, K., Tarantola, A., 1995. Monte carlo sampling of solutions to inverse problems. Journal of Geophysical Research: Solid Earth 100, 12431–12447. URL: https://doi.org/10.1029/94JB03097, doi:10.1029/94JB03097.

Neal, C., Brantley, S., Antolik, L., Babb, J., Burgess, M., Calles, K., Cappos, M., Chang, J., Conway, S., Desmither, L., et al., 2019. The 2018 rift eruption

and summit collapse of Kīlauea Volcano. Science 363, 367–374. URL: https://doi.org/10.1126/science.aav7046, doi:10.1126/science.aav7046.

Patrick, M., Wilson, D., Fee, D., Orr, T., Swanson, D., 2011. Shallow degassing events as a trigger for very-long-period seismicity at Kīlauea Volcano, Hawai'i. Bulletin of Volcanology 73, 1179–1186. URL: https://doi.org/10.1007/s00445-011-0475-y, doi:10.1007/s00445-011-0475-y.

Patrick, M.R., Anderson, K.R., Poland, M.P., Orr, T.R., Swanson, D.A., 2015. Lava lake level as a gauge of magma reservoir pressure and eruptive hazard. Geology 43, 831–834. URL: https://doi.org/10.1130/G36896.1, doi:10.1130/G36896.1.

Patrick, M.R., Orr, T.R., Swanson, D.A., Elias, T., Shiro, B., 2018. Lava lake activity at the summit of Kīlauea Volcano in 2016. Technical Report. US Geological Survey. URL: 10.3133/sir20185008, doi:https://doi.org/10.3133/sir20185008.

Rabinovich, A.B., 2010. Seiches and harbor oscillations, in: Handbook of coastal and ocean engineering. World Scientific, pp. 193–236. URL: https://doi.org/10.1142/9789812819307_0009, doi:10.1142/9789812819307_0009.

Richardson, J.P., Waite, G.P., 2013. Waveform inversion of shallow repetitive long period events at Villarrica Volcano, Chile. Journal of Geophysical Research: Solid Earth 118, 4922–4936. URL: https://doi.org/10.1002/jgrb.50354, doi:10.1002/jgrb.50354.

Rivalta, E., Segall, P., 2008. Magma compressibility and the missing source for some dike intrusions. Geophysical Research Letters 35. URL: https://doi.org/10.1029/2007GL032521, doi:10.1029/2007GL032521.

Segall, P., 2010. Earthquake and Volcano Deformation. Princeton University Press.

Shima, M., 1958. On the second volcanic micro-tremor at the volcano Aso. Disaster Prevention Research Institute, Kyoto University, Bulletins 22, 1–6.

Sneddon, I.N., 1946. The distribution of stress in the neighbourhood of a crack in an elastic solid. Proceedings of the Royal Society of London. Series A. Mathematical and Physical Sciences 187, 229–260. URL: https://doi.org/10.1098/rspa.1946.0077, doi:10.1098/rspa.1946.0077.

Wilson, B.W., 1972. Seiches, in: Advances in hydroscience. Elsevier. volume 8, pp. 1–94. URL: https://doi.org/10.1016/B978-0-12-021808-0.50006-1, doi:10.1016/B978-0-12-021808-0.50006-1.

Wilson, D., Elias, T., Orr, T., Patrick, M., Sutton, J., Swanson, D., 2008. Small explosion from new vent at Kīlauea's summit. EOS, Transactions American Geophysical Union 89, 203–203. URL: https://agupubs.onlinelibrary.wiley.com/doi/abs/10.1029/2008EO220003, doi:10.1029/2008EO220003.

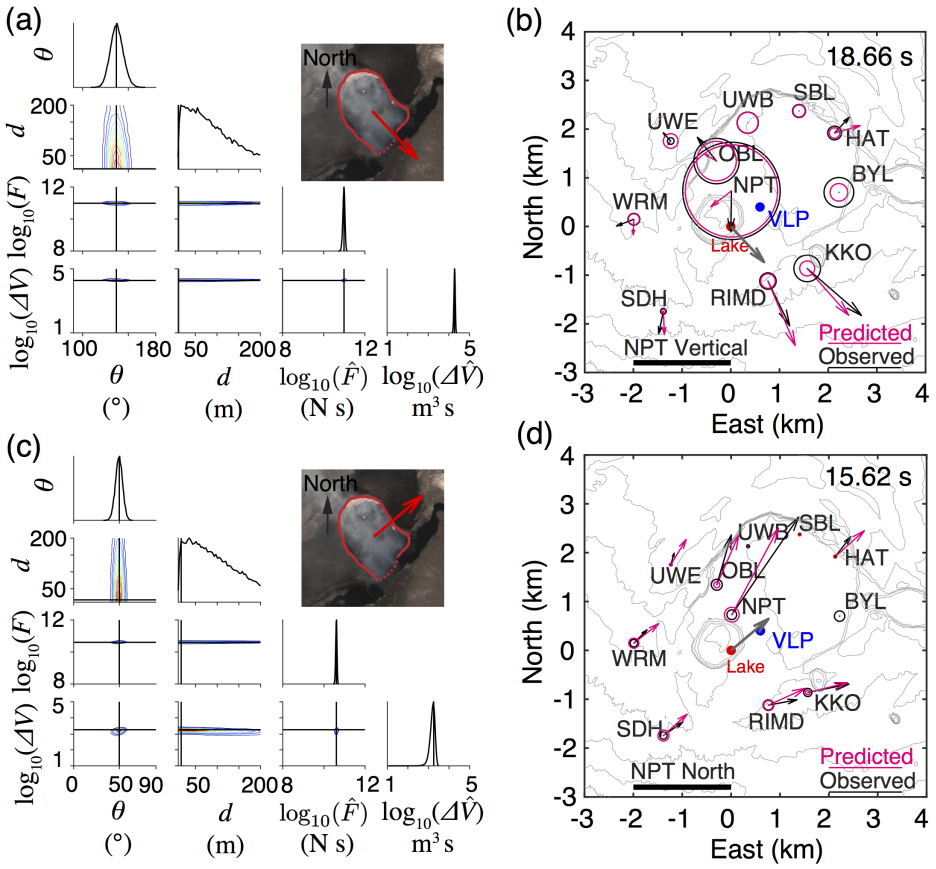

Figure 5: Inversion of sloshing modes for event on 2018-5-3T03:32:40. (a) Correlation plots of model parameters for 18.68 s mode. The vertical and horizontal black lines indicate the MLE model. The red arrow in the upper right map indicates the MLE force orientation. (b) Observed surface displacements compared to predictions from the MLE model for the 18.66 s mode. The gray arrow marks the MLE force orientation. (c) and (d) Same as (a) and (b) but for the 15.62 s mode. The MLE orientations of inferred horizontal forces for both sloshing modes are consistent with the axes of the crater.

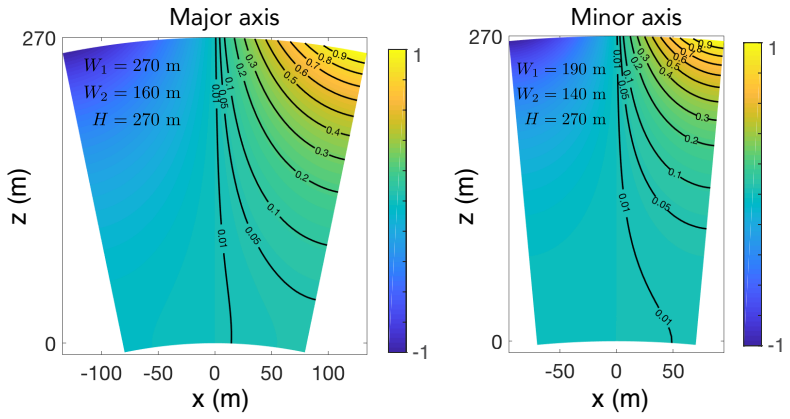

Figure 6: Pressure perturbations (normalized by maximum value) for sloshing modes along (a) major and (b) minor axes. Perturbations are confined near the free surface, indicating that both sloshing modes are in the short wavelength or "deep water" limit.

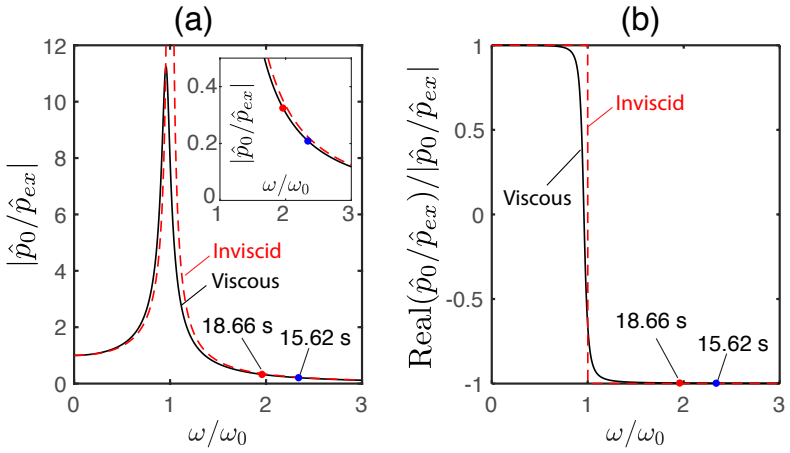

Figure 7: (a) $|\hat{p}_0/\hat{p}_{ex}|$ as a function of normalized angular frequency ω/ω_0 for an oscillator with $T = 38.12$ s and $Q = 11$ (accounting for magma viscosity). The red dashed line indicates the inviscid case. Note the amplification near ω_0 and that the two sloshing modes (18.66 s and 15.62 s) have higher frequencies than ω_0. (b) Normalized real part of $\hat{p}_0/\hat{p}_{ex}$. Note the negative sign of the real parts of $\hat{p}_0/\hat{p}_{ex}$ at two sloshing frequencies due to the phase lag between forcing and response. Shown for $\gamma^{-1} = 0$ (negligible buoyancy).

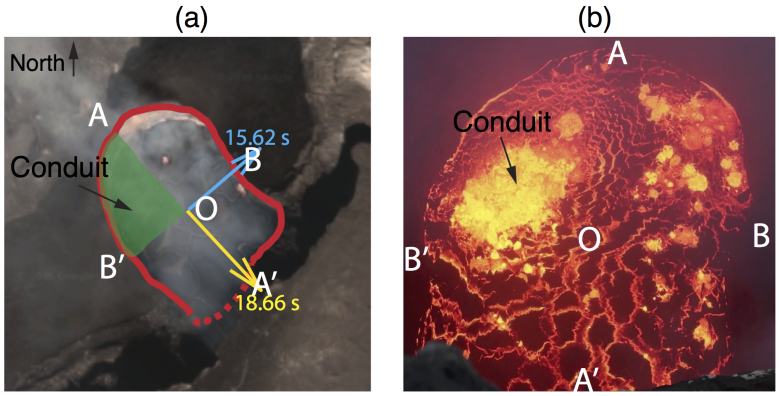

Figure 8: (a) Predicted conduit location by two sloshing modes (the green quadrant). The two arrows indicate the orientation of the horizontal force when the reservoir experiences an inflation (uplift in vertical displacement) for two sloshing modes. (b) Image of the lava lake showing an actively convecting region on May 7, 2018 when the lava lake level was near the bottom. The image is a screen shot (at 15 s from the start) of the video filmed by scientists from Hawaii Volcano Observatory (HVO) (HVO, 2018), standing approximately at location A' and looking into the lava lake toward A, as shown in (a).

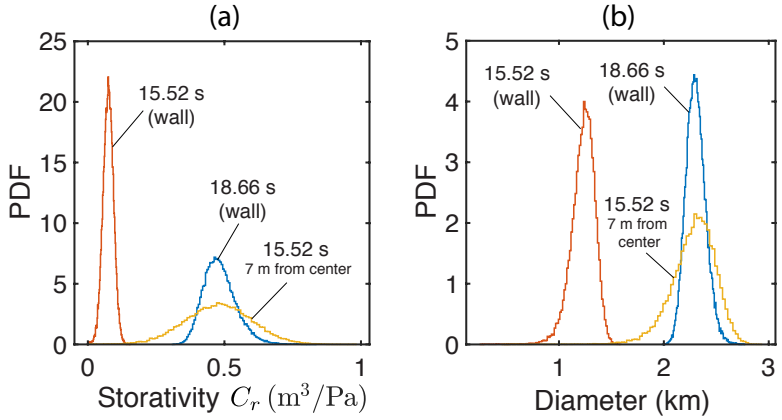

Figure 9: (a) Posterior probability function (PDF) of reservoir storativity C_r for two sloshing modes. (b) Reservoir diameter constrained by two sloshing modes assuming a spherical reservoir. By setting the conduit location to 7 m from the center along the minor axis and near the wall along the major axis, the MLE of storativity and sphere diameter inferred from two sloshing modes match (yellow and blue lines). Note that results are shown for $\gamma^{-1} = 0$ (negligible buoyancy); accounting for buoyancy would increase storativity and diameter.